

Full-length paper

# Demonstration of atomic resolution Z-contrast imaging by a JEOL JEM-2010F scanning transmission electron microscope

E. M. James<sup>1</sup>, N. D. Browning<sup>1</sup>, A. W. Nicholls<sup>2</sup>, M. Kawasaki<sup>3</sup>, Y. Xin<sup>1</sup> and S. Stemmer<sup>1</sup>

<sup>1</sup>Department of Physics (M/C 273), University of Illinois at Chicago, 845 W Taylor Street, Chicago, IL 60607–7059,

<sup>2</sup>Research Resources Center (M/C 937), University of Illinois at Chicago, 835 S. Wolcott Avenue, Chicago,

IL 60612–7341, USA and <sup>3</sup>JEOL Ltd, 1–2 Musashino 3-chome, Akishima, Tokyo 196, Japan

**Abstract** The collection of atomic resolution Z-contrast images, using an annular dark-field detector, has until recently been exclusively performed using the dedicated scanning transmission electron microscope (STEM). Here, preliminary results demonstrate the capability of performing this technique with a 200 kV FEGTEM, featuring a Schottky-emission electron gun. As in the dedicated STEM, the microscope's spatial resolution limit, for both Z-contrast imaging and chemical micro-analysis experiments, depends on the objective lens spherical aberration and the source brightness. Images from a number of materials indicate sub-2 Å Z-contrast resolution. In addition, the instrument exhibits probe stability sufficient to observe 1.6 Å lattice fringes in coherent convergent beam electron diffraction (CBED) patterns. Using an electron Ronchigram, a spherical aberration coefficient of 0.5 mm has been measured in STEM alignment for one particular pole-piece. Therefore, higher spatial resolution than that observed here may be possible with a further optimized instrument.

**Keywords** scanning transmission electron microscope, atomic resolution Z-contrast imaging

**Received** 30 March 1998, accepted 31 July 1998

## Introduction

The most widely used method for high-resolution studies of materials in transmission electron microscopy (TEM) is phase-contrast imaging [1–3]. As the name implies, this technique relies on the coherent interference of scattered beams and this interference directly produces the image contrast. A relatively large area of the specimen is illuminated and interpreting the contrast can provide information on the atomic structure of crystals, defects and interfaces. However, there are two main problems with this method, both of which lead to contrast in the image which does not relate in a clear manner to the atomic arrangement under study. Firstly, the interaction of the incident electrons in the specimen can be complicated. Multiple scattering and absorption events affect the image intensity in a non-trivial way. Secondly, the unavoidable aberrations of the objective lens impose phase changes which differ

between scattered beams, thus directly affecting the contrast. Consequently, it is difficult to interpret phase-contrast images at the highest resolutions. Image artifacts and contrast-reversal effects may conspire to make the location of an atomic column appear bright or dark in an image. To be able to predict which will be the case, accurate *a priori* information of such details as the exact specimen thickness and electron-optical settings of the microscope are required. Usually it is necessary to resort to extensive simulation of the image formation process, using trial structures, to arrive at a likely, though not unique atomic arrangement [3]. As the accuracy of simulations is drastically reduced in the region of interfaces and defects, such a method may not be the optimum approach to their study.

Recently it has been possible, using a dedicated scanning transmission electron microscope (STEM), to perform a

process of incoherent imaging at a resolution comparable to that obtained with the phase contrast method in a high-resolution conventional TEM or CTEM, i.e. at atomic resolution [4,5]. These incoherent images are generally trivial to interpret in terms of an atomic arrangement if the specimen is crystalline and viewed down a zone-axis. The method requires the focusing of a cross-over, or probe, at a specimen, which has a spatial extent smaller than the atomic spacings within the specimen. For many materials, in major zone-axis orientations, this translates to an upper limit on the probe size of the order of 2 Å. STEM incoherent imaging has shown great promise, for instance, in determination of the projected grain boundary structure in semiconductors, ceramics, high  $T_C$  superconductors and other specimens with atoms of medium to high atomic number.

The incoherent imaging method involves collection of the scattering over an annular post-specimen detector centred on the optic axis (Fig. 1). Theoretical analyses of this STEM annular dark-field (ADF) imaging have been given elsewhere [6–8]. Most notably, when considered mathematically, the image intensity for crystalline specimens viewed down a zone axis is given by the convolution of a specimen function with the probe intensity distribution. This result means that there is an absence of coherent, contrast-reversal effects in experimental images: a localized bright area of the image corresponds directly to an

atomic column in the structure. The maximum attainable resolution is significantly improved over that obtained with the conventional phase-contrast technique. This is because, in the latter, the image intensity is a convolution of the probe *amplitude*, not its intensity, with the specimen object function. Also, it can be shown that for the high detection angles employed in the annular scheme, the specimen function approaches that due to Rutherford scattering and is approximately proportional to the square of the projected atomic potential [6–9], and hence to the atomic number,  $Z$ . Individual columns are therefore also imaged with a high degree of chemical sensitivity (or  $Z$ -contrast).

An additional advantage of the incoherent imaging method in STEM mode is that many inelastic scattering experiments, able to reveal a wealth of composition and bonding information on the specimen, can be performed simultaneously. Such experiments include EELS [10,11] and energy dispersive X-ray spectroscopy (EDS) [12]. Because of the annular detector arrangement in  $Z$ -contrast imaging, the low angle inelastic EELS signal can be collected simultaneously with an atomic resolution image. There is no difference between alignment of the microscope for imaging and for analysis. Hence, the position of the probe with respect to the specimen can be determined with ångstrom accuracy and the analytical information correlated with a structural feature observed in the image.

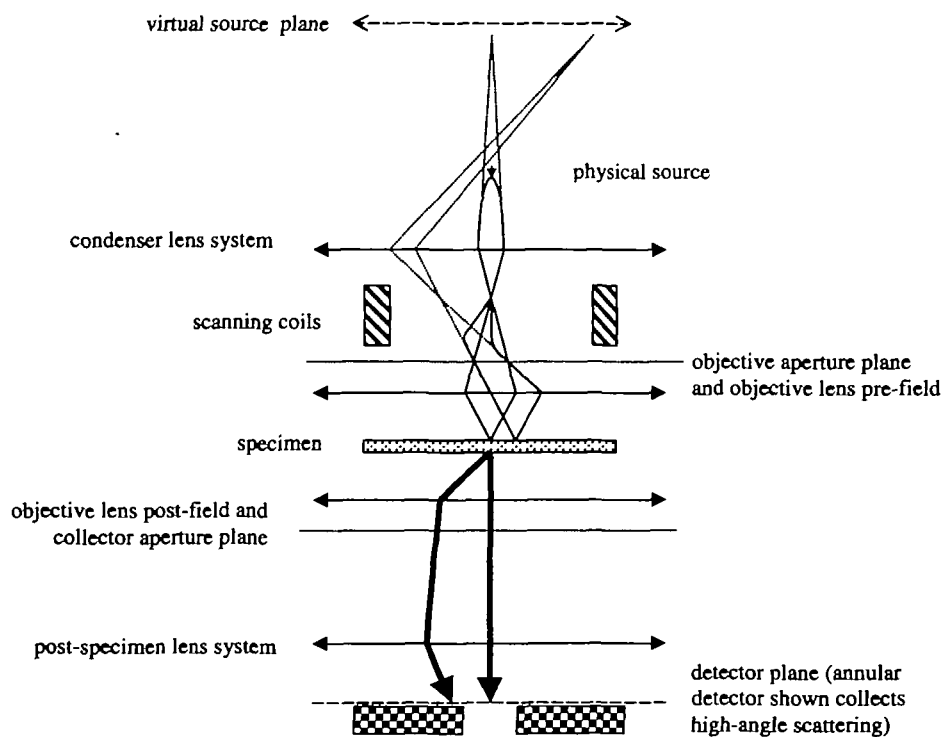


Fig. 1 Schematic of the dedicated STEM: electrons travel from top to bottom. Scanning coils control the position of the probe (a demagnified image of the virtual source) and, at each probe position, the scattered intensity can be measured at a variety of detection angles. For  $Z$ -contrast imaging and annular detector is used. Pre-specimen real ray (virtual ray) paths are shown by narrow solid (dashed) lines. Post-specimen intensity, scattered to a given angle, is shown by the broad lines.

High spatial resolution is ensured because of the small probe dimensions. The STEM method, using the Z-contrast image as a basis for analysis, therefore allows a correlation of a number of microscopy techniques at atomic resolution [13–15].

These STEM techniques have, to date, yielded results for a number of materials, using the dedicated 100 kV and 300 kV STEM instruments manufactured by Vacuum Generators Ltd (for example [5, 15–17]). However, any microscope with the capability of forming a probe of sufficient brightness can be employed in a similar fashion. Installation of a suitable annular detector is the only modification necessary. In this paper we consider the potential of Z-contrast imaging, using a contemporary incarnation of the JEOL JEM-2010F in probe-forming mode. The relevant capabilities of the JEM-2010F are shown to approach closely those of the dedicated STEM. For the instrument employed in this study, the images obtained show that the relevant resolution limit is below 2 Å. Additionally, analysis of the microscope stability and probe brightness suggests the possibility of further improvement of the resolution limit by use of a (currently available) higher-resolution objective lens pole-piece for the objective lens.

### Utilizing Z-contrast imaging in STEM

An understanding of the formation of Z-contrast images is useful in order to recognize the validity of, and also the limitations to, the simple interpretation scheme previously outlined. This then allows the conditions required for incoherent imaging on a microscope such as the JEOL JEM-2010F to be determined. Sufficient resolution and incoherence are required, such that the areas of high image plane intensity correspond to the positions of atomic columns and additionally, that higher intensity columns contain elements of higher atomic number.

First we consider the effect of forming a stationary probe at the surface of a thin crystalline specimen. In the far field, a coherent convergent beam diffraction (CBED) pattern will be formed (Fig. 2). High-resolution information is expressed in this pattern by interference between the diffracted beams [18]. By integrating the CBED pattern over the angular range of a particular detector, we arrive at the intensity of a single STEM image pixel. As the probe is then scanned, it is the CBED interference intensity variation which yields the contrast of the high resolution image (in this case, showing atom column positions) [18,19]. For Z-contrast imaging at 200 kV, the detector integration takes place over an annulus with inner and outer angles of around 40 mrad and 100 mrad respectively.

In determining the image contrast a number of methods can be employed to take account of the scattering of electrons by the specimen (i.e. the solution of the Schrödinger equation in the specimen electrostatic potential). Firstly, the kinematical approximation can be taken, which

assumes single scattering [1–3]. Unfortunately, this only holds for vanishingly thin specimens. For most practical applications, the dynamical effects of multiple scattering have to be taken into account. One computational way to do this is by using the multislice method [20]: this solves the problem by propagating the electron wave between thin slices of the specimen which each scatter electrons kinematically. The method can be used to simulate STEM Z-contrast images if the effects of thermal diffuse scattering are included [21–25]. A drawback to the multislice simulations is that they are computationally intensive since STEM image formation is a serial process and multislice calculations have to be performed for each position of the probe, to yield an integrated CBED intensity over the annular detector, for every image pixel in turn.

An alternative approach is to consider diffraction in the specimen in terms of Bloch wave solutions of the Schrödinger equation [6–9]. Particularly in the case of Z-contrast imaging, the Bloch wave formalism can be usefully employed to improve the physical understanding of contrast formation. For instance, when the Bloch states are integrated over the probe angles of incidence, it can be shown that the 1s-type states bound to the atom columns are most strongly excited [5]. This physically represents channeling of the electron beam along the atomic columns as it propagates through the crystal [5,26] and explains the ability to observe interpretable Z-contrast images up to relatively high specimen thickness. The interference effects between neighbouring 1s states are minimized by the geometry of the ADF detector resulting in incoherent structural imaging [8,9]. A small detector, such as an axial bright field detector, has a large coherence envelope and so small interference features are observed in phase contrast images. However, an ADF detector has a very small coherence envelope, because the features are integrated over it. Coherent interference effects between neighbouring states can be reduced arbitrarily, by increasing the detector inner angle. This is of course done at the expense of reduced current collection and image intensity.

The above arguments show that the ADF detector geometry acts as a filter. The integrated information it collects contains little signal due to transverse interference between the Bloch states, and channeling along the atomic columns prevents probe spreading in the specimen. Additionally, it has been shown that scattering at high angle is more favorable from 1s-type Bloch states with high kinetic energy and that this weighting yields image intensities proportional to  $Z^2$  as the inner detector angle tends to 180° [9]. The overall result is that the ADF detector geometry yields an image intensity which approximates very closely the definition of incoherent imaging,

$$I(\mathbf{r}) = |a(\mathbf{r})|^2 \otimes o(\mathbf{r}) \quad (1)$$

where  $a(\mathbf{r})$  is the probe complex amplitude which is convolved with  $o(\mathbf{r})$ , an object function proportional to

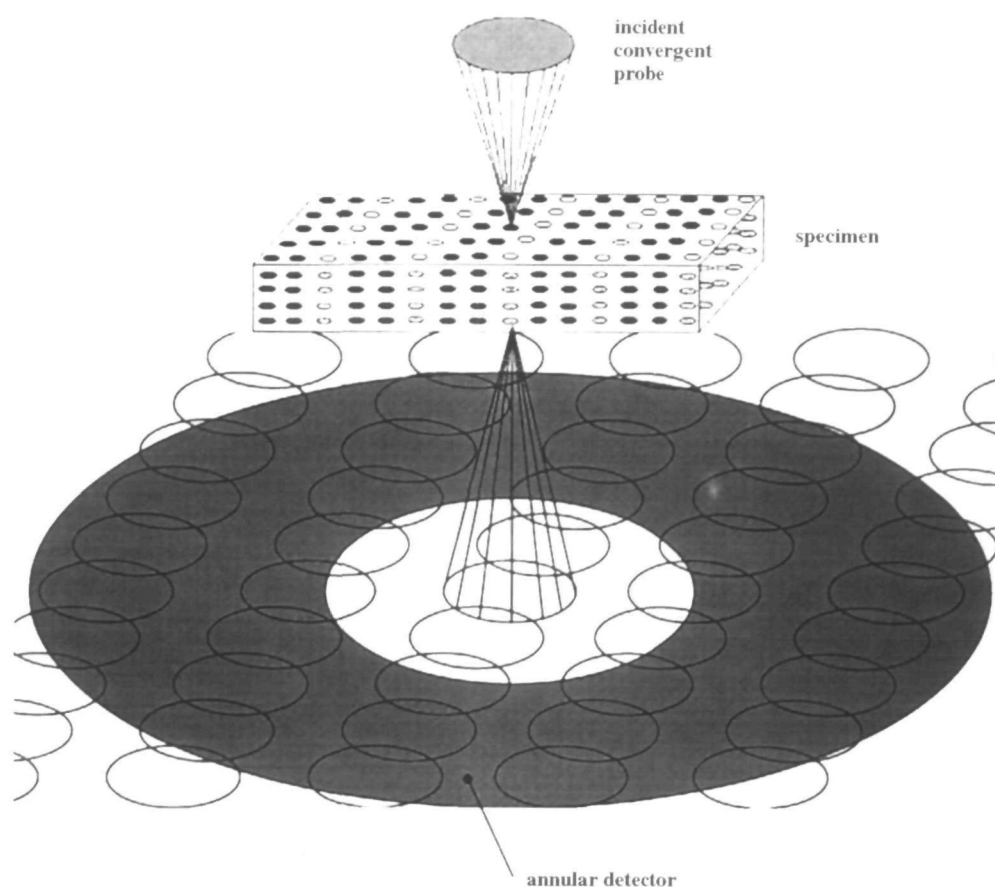


**Fig. 2** Schematic diagram of a STEM convergent-beam diffraction (CBED) pattern, showing how diffracted discs fall across an annular detector (not to scale). As the probe is scanned, intensities in the disc overlap regions oscillate, expressing specimen information at high spatial frequency. The Z-contrast image is the total signal detected on the annulus, as a function of the probe position.

the square of the projected atomic potential. It should be stressed here that it is the final integration across an annular detector which destroys interference effects in the Z-contrast image; the probe itself must be highly coherent in order to resolve spatially separated parts of the specimen. The term 'incoherent imaging' therefore does not refer to the STEM probe formation process. In fact, a necessary, but not sufficient, condition for resolution of a particular lattice spacing is that the illumination coherence angle exceeds the Bragg angle corresponding to that spacing.

The above analysis does not include the effects of interference between Bloch states along the individual atomic columns. The large annular detector is only effective at suppressing coherence effects in the transverse direction. Consequentially, the theory predicts the oscillation of scattered intensities, dependent on the specimen thickness. However, phonons with wavevectors parallel to the beam direction tend to break this longitudinal coherence and dampen the intensity oscillations [5–8]. Residual correlations become most important when the spacing of atoms is different in neighbouring columns, though this effect does not lead to contrast reversal in

the image and so the interpretation remains simple in comparison to that with the phase-contrast method. Nevertheless, care must be taken when interpreting images in terms of the chemical composition of aperiodic regions of the specimen, such as at interfaces. Interpretation problems also are significant as the spacings to be resolved approach the resolution limit, given approximately by the probe size. In this case, the probe imposed information limit, which truncates the Fourier spectrum of the signal passed to the image, can also cause a small but significant alteration of the intensity maxima separations compared to the real column spacings in the material.

One final matter to bear in mind is the form of the probe function itself. Given incoherent imaging according to Equation 1, it is still necessary to assume that the probe intensity has a single, localized maximum in order to trivially interpret the image in terms of the atomic structure. At the Scherzer condition the probe is approximately Gaussian in shape; however, at certain underfocus conditions the probe will have significant tails (areas of intensity at a distance from the central maximum). Fortunately, in practice it is found that the Scherzer condition is very

easy to locate. Spurious intensities, caused by the tails, are negligible in comparison to the peaks at the column sites until the image is visibly out of focus. It may even be practical to utilize the narrowing of the central probe peak under these under-focus conditions, and reconstruct specimen information at higher spatial frequencies [9].

In summary, the Z-contrast technique is a close approximation to incoherent imaging (Eq. 1). The geometry of the detector and the coherence-breaking effect of phonons efficiently suppresses the signal from coherently interfering scattered beams. In practice, Z-contrast images are extremely easy to interpret in terms of the atomic structure. Atomic column positions can directly be found to an accuracy determined by the probe size, which limits the transfer of very high spatial frequencies. Care must be taken in assigning chemical composition to atomic columns directly from the intensities, since the further approximation of their proportionality to  $Z^2$  is only valid for a detector inner angle tending to  $180^\circ$  and is modified by highly damped, thickness dependent oscillations. However, there is significantly more analytical information available than in a bright-field phase-contrast image. The ability to simultaneously collect EELS spectra, without realignment of the microscope, expands this analytical capability still further.

### The JEOL JEM-2010F STEM

Figure 3 shows the electron optical arrangement of the JEOL JEM-2010F, when operated as a STEM. In the configuration described here, the gun (electrostatic) lens, both condenser lenses and the objective lens pre-field are used to form a probe, with the desired demagnification level of around one thousand. A cross-over is formed in the gun area, above a differential pumping aperture, by exciting the electrostatic lens above its nominal strength. With C1 run near maximum excitation, a large geometrical demagnification of the electron source is ensured. C2 is then employed to form a cross-over approximately half-way between itself and the objective lens pre-field. The objective mini lens is not used in this configuration. The scanning attachment drives alignment coils, situated between the condenser C2 lens and the objective. With this arrangement, the aperture used to define the illumination maximum angle of incidence is not at the back focal plane of the objective. Despite this position, it will be referred to as the STEM objective aperture. The angular range of probe-forming beams therefore is a function of the exact settings of the gun, C1 and C2 in addition to the aperture size. This STEM electron optical arrangement is the standard factory configuration and was used to obtain the results described in this paper. It is not yet known whether a more favourable alignment for atomic-resolution Z-contrast imaging can be found. The particular microscope used for imaging was a JEOL demonstration instrument equipped with an analytical pole-piece and Gatan parallel

EELS model 666. In CTEM-mode, the focal length is 2.7 mm: the spherical and chromatic aberration coefficients, quoted by the manufacturer, are 1.0 mm and 1.8 mm respectively. An important property of this instrument is its ability to switch easily between CTEM and STEM operation. This allows a very large number of different experiments to be performed on the same specimen, without transferring it between microscopes. Also, alignment and tilting of the specimen is most often easily achieved by looking at the CTEM image in bright field and diffraction modes. TEM studies of, for instance, the grain boundaries of polycrystalline materials are simplified in this way with preliminary alignment in CTEM.

### Instrumental considerations for high-resolution STEM

When comparing the performance of a particular instrument in CTEM and STEM imaging modes, it is necessary to consider the concept of reciprocity. This theorem can be applied to electron optics [27] and, in particular, to the relationship between STEM and CTEM imaging. It shows, for elastic scattering, the equivalence between CTEM illumination tilt and STEM detector angular position, and between position at the CTEM detector plane and the effective STEM source position (controlled by a scanning system). As a result, it is possible to form the same type of image using either instrument. In practice though, one form of TEM may be a much more efficient method. For instance, in the bright-field mode it is not possible to achieve STEM image signal-to-noise ratios as high as those in CTEM. This is because a bright enough probe cannot be formed. Also, reciprocity does not guarantee a particular method will be equally as easy to configure for both microscope arrangements. A STEM ADF detector is much simpler to employ than the equivalent hollow-cone CTEM illumination system. Because of these factors, an instrument able to operate at atomic resolution in both scanning and conventional imaging modes will have the widest range of applications.

The JEOL JEM-2010F is one of a number of microscopes, originally designed as a CTEM, which has all the necessary electron optical components to act as a dedicated STEM by scanning a probe at the specimen (Fig. 3). However, it can be seen from reciprocity that the critical instrumental parameters, in order to achieve atomic resolution in STEM, are different from those for conventional imaging. In the former, the probe brightness must be maximized. Factors that determine this are the intrinsic brightness of the electron source itself; the arrangement and aberrations of the probe-forming electron optics, in particular the amount of geometrical source demagnification and the spherical aberration of the objective lens pre-field; and the influence of mechanical and electrical instrumental instabilities.

The microscope under study here uses a Schottky field

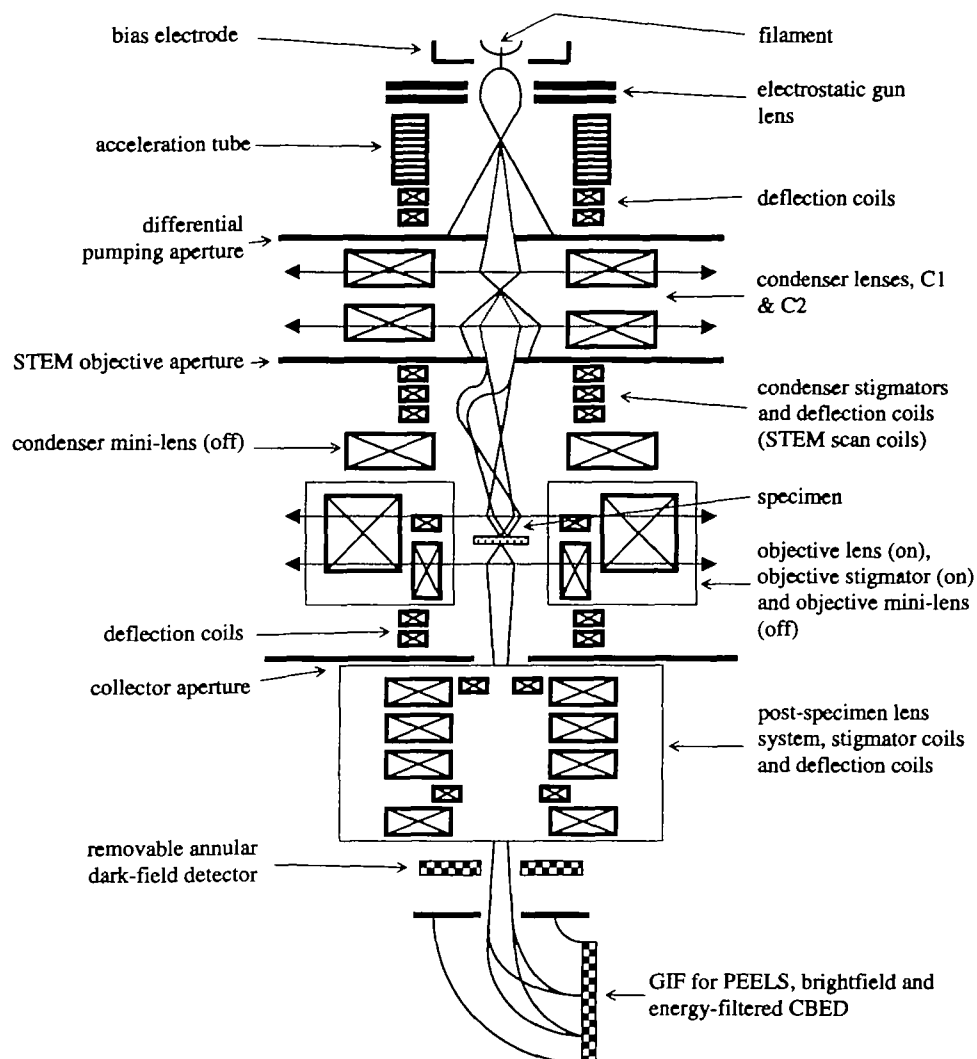


**Fig. 3** Electron optical arrangement of the JEOL JEM-2010F STEM. To form the optimum probe, the gun lens and C1 are run at high excitation to ensure a large geometrical demagnification of the source. The post-specimen lens system allows the camera length to be changed easily. This has the effect of altering the effective angular size of the detectors.

**Table 1.** Comparison between the Schottky emission and cold field emission (CFE) electron sources.

	Schottky source	Cold field emission (CFE) source
Cathode material	Zr/W	W
Field at cathode apex	500 MV m <sup>-1</sup>	5000 MV m <sup>-1</sup>
Cathode temperature	1800 K	300 K
Maximum recommended gun pressure	10 <sup>-9</sup> mbar	5×10 <sup>-11</sup> mbar
Approximate beam energy spread	0.6 eV	0.3 eV
Reduced source brightness	2×10 <sup>8</sup> Am <sup>-2</sup> sr <sup>-1</sup> V <sup>-1</sup>	2×10 <sup>9</sup> Am <sup>-2</sup> sr <sup>-1</sup> V <sup>-1</sup>

emission tip of the ZrO/W <100> type. Table 1 lists the nominally quoted properties of this source, in comparison to the cold field emission (CFE) tungsten <310> type, which is used in a dedicated STEM. In its favour, the Schottky gun operates well in a relatively easy to obtain ultra-high vacuum of a few 10<sup>-10</sup> mbar and is also exceptionally long-lived. However, the reduced brightness

(expressed as current per unit area, per unit solid angle, per volt) is usually quoted to be up to an order of magnitude inferior to that of CFE [28,29]. This suggests that the effective probe brightness, and thence the STEM resolution limits, of a microscope with a Schottky gun will be inferior to those of a CFE-equipped instrument, provided that the source brightness is a dominant factor.

Put another way, the maximum amount of current, available for a given probe-size, is expected to be less when using a Schottky source.

Exploring the above premise in more detail, we consider conservation of reduced brightness (brightness per unit accelerating voltage) along the microscope column [1]. In this way, a quantitative estimate of the maximum attainable current for a particular probe size can be found, for both a Schottky and a dedicated CFE STEM system. In the simplest hypothetical case, the probe-forming optical system consists of a source imaged by an objective lens with an aperture stop. Starting from a probe size that is limited by spherical aberration, the effect of making the aperture smaller and reducing the probe convergence angle reduces the size, but at the price of reduced current. However, for very small angles the probe is diffraction limited and it is found that the probe current is a constant multiple of the reduced brightness [30]. It is the current density which then falls with convergence angle since the probe (Airy disc) diameter then increases. Therefore, at the optimum aperture angle, the smallest probe has an intensity full-width-half-maximum (FWHM) dependent on the spherical aberration coefficient of the lens, but a current determined solely by the reduced brightness, since this is just the point at which the probe becomes diffraction limited.

Given the accepted brightness values from Table 1, a CFE equipped microscope can focus a current, into an optimum diffraction limited probe, that is around ten times greater than that possible using a Schottky emitter. However, the experimentally measured probe currents for the Vacuum Generators HB501/HB601/HB603 dedicated CFE STEMs, when set for an optimum probe size, are around one order of magnitude less than the predicted 200 pA [31]. This indicates the influence of instabilities and the imperfections of the gun electron-optics in reducing the effective brightness in these microscopes. It also suggests that, in principle, a Schottky emission microscope is approximately capable of matching the performance of contemporary dedicated STEMs. JEOL JEM-2010F experimental images presented here were obtained with a probe current of 20 pA ( $\pm 5$  pA) [32]; a level which is in line with this expectation. This current was measured by imaging the probe onto an isolated, current-calibrated phosphor screen, using the post-specimen lens system.

A second potential disadvantage with the Schottky source is the electron energy distribution of around 0.6 eV (in comparison to under 0.3 eV for CFE). The main effect of this larger spectral width is a reduction in the energy resolution of parallel EELS spectra. However, to ensure incoherence in the EELS signal in the dedicated STEM, a large collector aperture must be used [33]. In this case, chromatic aberrations of the spectrometer, not the source energy spread, dominate the energy resolution. When using a FEGTEM, such as the JEOL JEM-2010F,

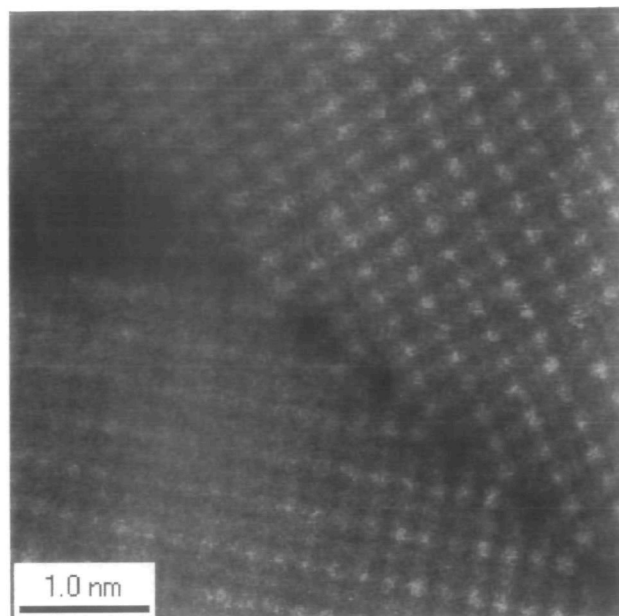


**Fig. 4** STEM annular dark-field image of a  $\langle 110 \rangle$  tilt grain boundary in  $\text{SrTiO}_3$ . Strontium columns appear brighter than those of titanium due to an approximate proportionality of the contrast with the atomic number squared. Sub-2 Å resolution is exhibited.

the post-specimen lenses (CTEM projector lenses) can be used to alter the camera length significantly. The reduction in angle of inelastic scattering, incident on the spectrometer, means that aberrations are minimized without loss of signal. It has been possible, using a second JEM-2010F fitted with a Gatan Imaging Filter, to measure the width of the zero-loss EELS peak. In STEM alignment, the filter could be adjusted to yield a full-width half-maximum of just under 1 eV. By observing the features of a number of core-loss edges, it was clear that energy resolution at least of this order can be obtained throughout the spectrum.

In summary, the Schottky electron source has a lower intrinsic brightness than that of cold field emission. However, it is the probe brightness that is of crucial importance and, in current dedicated STEMs, this is lower by about an order of magnitude. If probe-blurring electrical and mechanical instabilities are satisfactorily minimized and gun electron optics aberrations do not dominate, a Schottky gun FEGTEM should exhibit similar experimental performance.

## Experimental images

Figure 4 shows a Z-contrast image of a  $\langle 110 \rangle$  tilt grain boundary in  $\text{SrTiO}_3$ , obtained with the JEOL JEM-2010F instrument operating as a STEM. The Sr and Ti columns are separated by 1.95 Å in this projection and clearly exhibit contrast dependent on atomic number. The specimen was polycrystalline, with a grain size of  $\sim 1$  μm. The acquisition time, for this and other images presented here, was  $\sim 20$  s (512×512 pixel image). In the dedicated

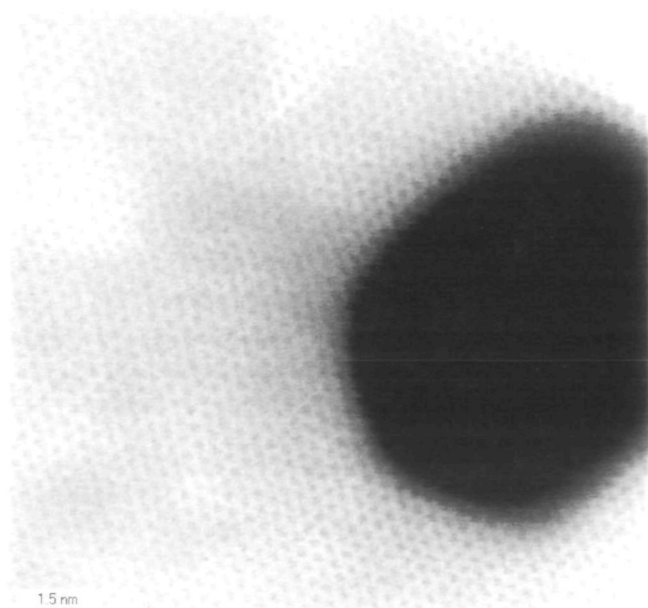


**Fig. 5** Z-contrast image of GaN <0001> in the vicinity of a 'nanopipe' void.

STEM, the lack of a eucentric stage and non-triviality of performing diffraction from small regions of specimen would make such an area of the sample difficult to locate and orient correctly. With the capability of switching to CTEM mode for specimen alignment, these problems were minimized. The images show that the instrument is capable of forming a useful, sub-2 Å probe and that interface structures can be imaged at atomic resolution.

Similar specimen illumination conditions were used to acquire Z-contrast images of gallium nitride <0001>, grown on a sapphire substrate. The hexagonal, honeycomb arrangement of this technologically interesting structure has spacings of 1.84 Å; each column comprises an evenly stoichiometric mixture of Ga and N atoms. The presence of many larger hexagonal structures – so-called nanopipes – were easy to locate in the Z-contrast image (Fig. 5). These pipes run through the whole structure and are, in fact, empty voids [34]. An area of the bulk GaN is shown at higher magnification in Fig. 6a. In places, the 1.84 Å atomic spacings appear to be just becoming resolved. Because of the hexagonal atomic arrangement, a periodicity corresponding to a 1.60 Å spacing must be present in the image to resolve individual columns (shown in Fig. 7). Taking the power spectrum of the raw image yields Fig. 6b. There are several peaks in the spectrum, far from the origin, due to instabilities at frequencies comparable to that of the rastering probe. Looking carefully, there are also peaks at the correct positions corresponding to the 1.60 Å specimen periodicity (indicated by arrows). Magnitude at these positions in the power spectrum explains the apparent resolution of atomic columns in certain image areas. These 1.60 Å periodicities

are the smallest so far observed in Z-contrast on the JEM-2010F, suggesting near optimum probe-forming conditions and relatively low instability levels in this case. To validate that the microscope can readily and routinely achieve this resolution more experimental images at many different scan rates should be taken to analyse the source of the instability peaks. The precise positioning of the magnitude indicated by the arrows, together with independent measurement of the crucial microscope parameters (see later sections) allows these peaks to be confidently associated with specimen periodicities. Notably, spot C is less visible above the noise than the equivalents A and B; this indicates a non-circularly symmetric probe intensity function.

A number of other imaging tests were carried out using other specimens. The resolutions obtained were seen to be sensitive to specimen illumination conditions, the level of amorphous surface layer, and changes in the microscope environment. In Z-contrast images, it was relatively straightforward to observe periodicities such as Si {220} (1.92 Å) and GaN {1 102} (1.89 Å).

### Probe stability and potential resolution limits

As previously emphasized, the stability and brightness of the probe is a crucial factor in determining the resolution in the STEM alignment. In order to consider these quantities in more detail, it is useful to introduce the concept of a Z-contrast transfer function,  $T(\mathbf{k})$ . This is a measure of how well features of a specimen are transferred to the image as a function of spatial frequency. The point where  $T(\mathbf{k})$  decays to zero is the resolution limit for this particular method. Probe size and current determine the form of the function, and a Fourier transform relates it to the probe intensity distribution. In turn, the probe size depends on two main factors: spherical aberration of the objective lens and the probe stability, or brightness. We wish to maximize the extent of  $T(\mathbf{k})$  in order to transfer image features at very high spatial frequency.

Given that it is, in principle, possible to reduce spherical aberration by better lens design, it is desirable to be able to separate out this factor in order to analyze the effect on  $T(\mathbf{k})$  of the source brightness and microscope instability levels. This can be done by direct observation of interference effects between Bragg diffracted beams in a CBED pattern, using a stationary probe. An estimation is obtained of the coherent imaging information transfer function,  $C(\mathbf{k})$  [35]: the ability of components of the illuminating beam to interfere, *irrespective* of whether their phases have been changed significantly by spherical aberration. It is the STEM equivalent of the function which modulates and attenuates the familiar phase-contrast transfer function of bright-field imaging. The CBED experiment was deemed especially useful here since it was not known precisely which factor limits the JEOL

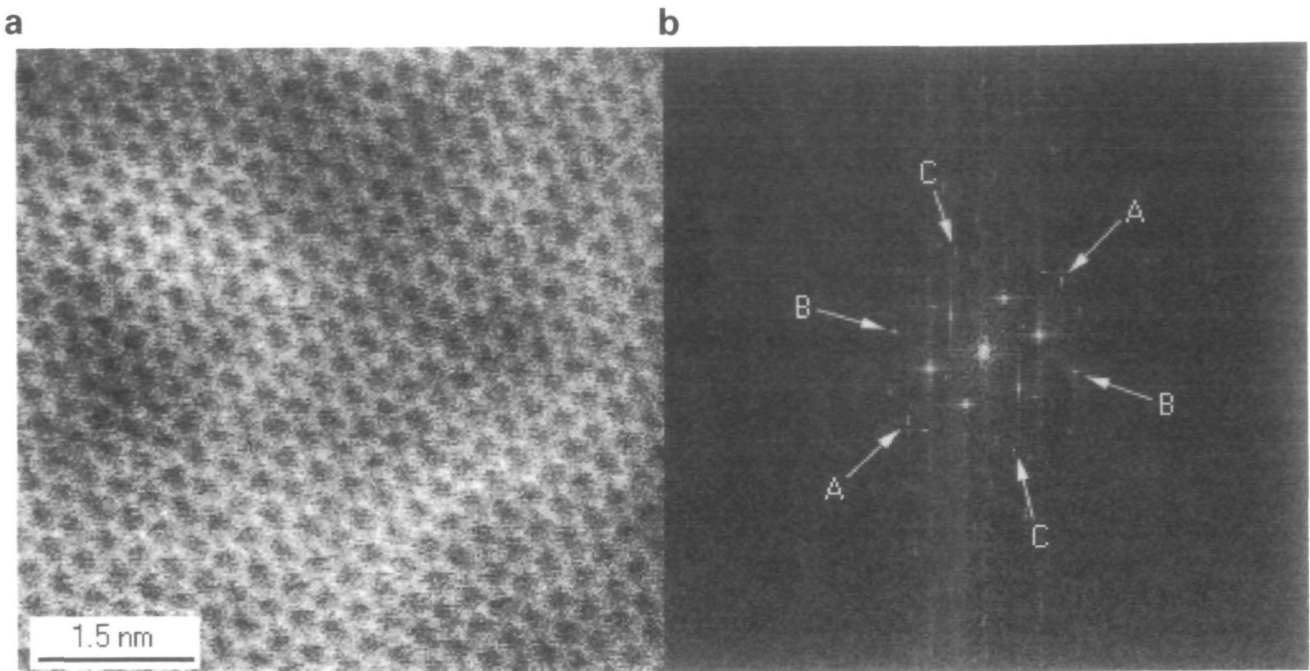


**Fig. 6** (a) High-resolution Z-contrast image of bulk GaN <0001>. (b) The associated power spectrum showing magnitude at points corresponding to a periodicity of 1.60 Å (labelled A, B and C). Other, spurious peaks are visible and may be indications of instabilities which affect the probe.

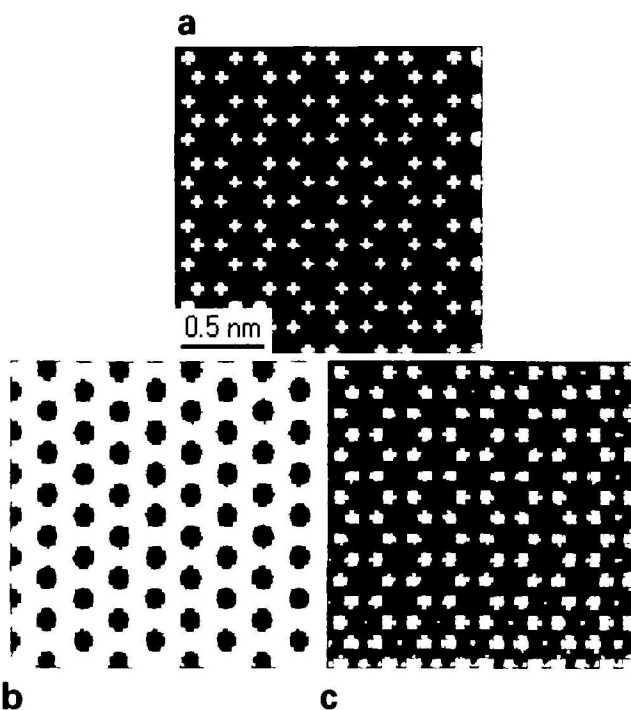


**Fig. 7** Fourier components of the GaN <0001> incoherent object function. (a) The object function consists of delta-functions at the column sites (here shown convolved with a Gaussian [FWHM of 1.0 Å]). (b) Object function when constructed from the lowest frequency  $0.36 \text{ \AA}^{-1}$  Fourier components only. (c) Object function when constructed from the  $0.36 \text{ \AA}^{-1}$  and  $0.63 \text{ \AA}^{-1}$  Fourier components only.

JEM-2010F STEM probe size (and hence, the form of the associated Z-contrast transfer function,  $T(\mathbf{k})$ ). In particular, the spherical aberration coefficient of the objective

lens in STEM-mode is not yet accurately known for all of the available pole-pieces. The nominally quoted value, for the 'analytical' pole-piece used for the imaging here, is 1.0 mm; a result which has been obtained from a series of CTEM experiments on different microscopes of the same specification. In STEM, the lens is excited differently and the crucial factors in imaging are those of the lens pre-field. The JEOL JEM-2010F is available with an 'ultra-high resolution' pole-piece. The measurement of its  $C_5$  coefficient in STEM operation is described in the following section. If the factors associated with  $C(\mathbf{k})$  (source and instabilities) are dominant, no improvement in Z-contrast resolution would be possible by selecting an objective lens with lower spherical aberration. Instead, remnant instabilities would have to be removed and, perhaps ultimately, an electron source installed with higher intrinsic brightness. Full knowledge of  $C(\mathbf{k})$  is therefore a direct measurement of the brightness which matters in STEM imaging, whether that be dominated by the source or by instabilities.

The CBED technique utilizes the fact that the intensity of features at the center of overlapping diffracted orders is independent of all spherically symmetric phase changes across the objective lens, such as defocus and spherical aberration [35,36]. This is because the parts of the beam that interfere have traversed diametrically opposite parts of the objective lens. Moving the probe applies a linear phase shift to the interference regions. In practice, a robust way to perform a complete quantification of the coherent information envelope,  $C(\mathbf{k})$ , involves acquiring a number of CBED patterns at different probe positions. The visibility

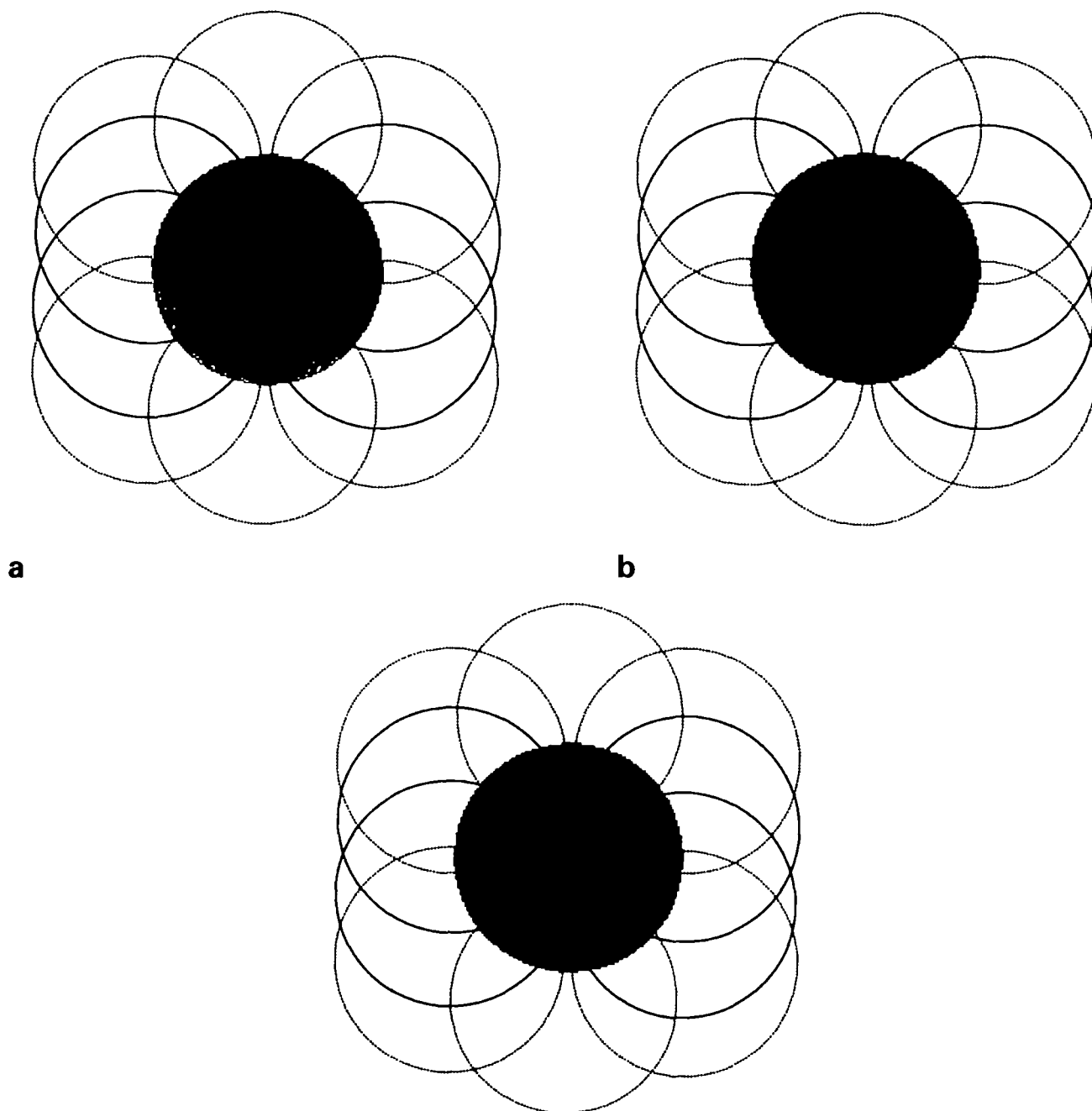


**Fig. 8** Simulated, defocused coherent CBED patterns for silicon  $\langle 310 \rangle$  (for clearness, only intensity in the central disc is displayed). The simulations assume an electron energy of 200 kV, an objective aperture subtending a semi-angle of 15 mrad, and a spherical aberration coefficient of 1.0 mm. Positions of the diffracted discs are shown by circles ( $\{1\bar{1}31\}$ -type – 4 circles with unbroken lines to left and right of (000);  $\{1\bar{1}3\bar{3}\}$ -type – dashed lines, also 4 circles on left and right;  $\{004\}$ -type – 2 dashed line circles at top and bottom). (a) An incoherent probe-broadening has been added with a FWHM of 0.84 Å (high spatial coherence). Fringes are seen in the overlaps between the (000) and  $\{004\}$  discs and between the (000) and  $\{1\bar{1}31\}$  discs. (b) An incoherent probe-broadening has been added with a FWHM of 1.50 Å (intermediate spatial coherence). Fringes between (000) and  $\{1\bar{1}31\}$  discs are visible. (c) An incoherent probe-broadening has been added with a FWHM of 1.84 Å (low spatial coherence). Fringes between (000) and  $\{1\bar{1}31\}$  discs are no longer present

of interference features at the center of the overlaps is then extracted using Fourier analysis [35]. Furthermore, a number of specimens would be required to sample  $C(\mathbf{k})$  over a sufficient range of spatial frequencies. However, in order to simply see whether interference is present, a

single CBED pattern, observed with a degree of defocus and suitable size of objective aperture will suffice. In this case, a number of interference fringes will be observed, approximately perpendicular to the relative reciprocal lattice vector,  $\mathbf{g}_{\text{rel}}$ , of the overlapping discs in question

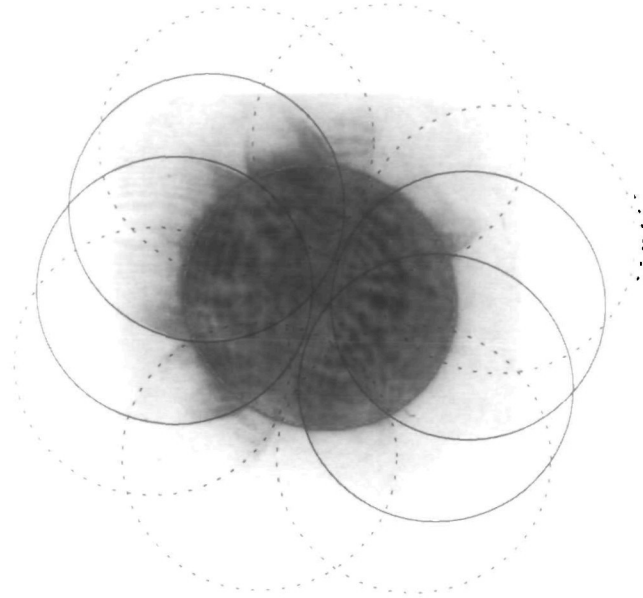


**Fig. 9** Experimental coherent CBED pattern from Si  $\langle 310 \rangle$  in the JEOL JEM-2010F. Defocus fringes are present between the (000) and  $\{131\}$ -type discs. An incoherent probe-broadening, due to instabilities and the finite source brightness means that the (000)/{004} overlap fringes are not visible. By comparing with the simulations of Fig. 11, the broadening FWHM is estimated to be around 1.5 Å.

[36,37]. A simple, geometric interpretation of these fringes is given in [38]. The fringe periodicity is determined by the amount of defocus and their visibility by the value of  $C(\mathbf{g}_{\text{rel}})$  [35, 36]. Therefore, simply observing fringes between discs separated by  $\mathbf{g}_{\text{rel}}$ , means that the coherence envelope must extend further than  $|\mathbf{g}_{\text{rel}}|$  in reciprocal space.

Figure 8 illustrates simulated coherent CBED patterns of Si  $\langle 310 \rangle$  for varying levels of probe coherence. The electron energy was 200 keV and a spherical aberration coefficient of 1.0 mm was assumed. An experimental pattern from the JEOL JEM-2010F is shown in Fig. 9. The pattern was observed at an over-focus setting and is quite complex because the available objective aperture was relatively large (15 mrad) and consequently a number of Bragg discs are overlapping. Also, spherical aberration causes the fringes to bend away from the overlap centers. Noticeable in the experimental patterns is the lack of interference between the zero-order and {004} discs. This means that  $C(\mathbf{k})$  does not have significant magnitude in reciprocal space extending as far out as  $|\mathbf{g}_{004}|$ . However, there is significant interference elsewhere, and in particular, the  $\{131\}/(000)$ -type overlaps exhibit fringing.  $|\mathbf{g}_{131}|$  corresponds to a specimen spacing of 1.64 Å and indicates that this resolution is likely to be obtained in Z-contrast imaging, provided the objective lens pre-field  $C_s$  is low enough. The direct detection of such fringes, simply by taking a photograph of the intensity reaching the microscope phosphor screen position, implies there is

probably enough current in the probe to yield adequate signal in the high angle scattering incident on an ADF detector. A numerical value for the probe brightness can be derived from this result. We assume, from the experimental evidence, that the function  $C(\mathbf{k})$  drops to zero quickly between  $\mathbf{k} = |\mathbf{g}_{131}|$  (0.61 Å<sup>-1</sup>) and  $\mathbf{k} = |\mathbf{g}_{004}|$  (0.74 Å<sup>-1</sup>). Taking  $|\mathbf{g}_{131}|$  to define the width of  $C(\mathbf{k})$ , this translates to an approximate probe diameter,  $d$ , of (1/0.61) Å (= 1.64 Å). The illumination convergence is then coherent over a semi-angle,  $\theta$ , of 7.64 mrad (half the Bragg angle). A probe current,  $I$ , of 20 pA is typical for this illumination condition. The probe brightness,  $B_r$ , due to incoherent broadening effects of the source size and instabilities alone, and per unit accelerating voltage,  $V$ , is then given by

$$B_r = \frac{4I}{\pi^2 \theta^2 d^2 V} \quad (2)$$

Substituting in the values yields an estimate for  $B_r$  of  $2.5 \times 10^7$  Am<sup>-2</sup> sr<sup>-1</sup> V<sup>-1</sup>. The precise value of  $B_r$  depends on the shape of the function  $C(\mathbf{k})$  and how its width is defined. For dedicated, cold field emission STEMs such as the VG HB501, estimates of  $B_r$  are also around  $2 \times 10^7$  Am<sup>-2</sup> sr<sup>-1</sup> V<sup>-1</sup> [30], for small probes: the brightness is generally limited by instabilities, rather than the source size [35]. The comparable level of probe brightness for the JEM-2010F means that Z-contrast imaging at resolutions under 1.5 Å is feasible. The main requirement is that electrical and mechanical instabilities are influencing the beam in parts of the column where they can be diminished by demagnification using a lens. Further investigation is needed to confirm whether this is the case. However, with this value for the probe brightness, the choice of a lens with as low a  $C_s$  coefficient as possible seems justified.

## Measurement of spherical aberration in STEM

The relatively high probe brightness and stability observed with the JEM-2010F means that the ultimate Z-contrast image resolution may be limited by spherical aberration of the objective lens. In other words, the transfer function,  $T(\mathbf{k})$ , decays to zero under the influence of the aberration before that of the brightness. For a FEGTEM it is unwise to assume that the STEM  $C_s$  constant is identical to that quoted by the manufacturer, for CTEM. It is the objective lens pre-field aberration that determines the probe size. Unless the lens behaves symmetrically, the STEM and CTEM  $C_s$  values will not be equal.

The spherical aberration coefficient has been measured on a JEM-2010F instrument fitted with an 'ultra-high resolution' pole-piece (nominal  $C_s = 0.5$  mm). This was not the same microscope used to obtain the Z-contrast images presented here. However, the probe brightness does not differ for identical microscopes, under the same

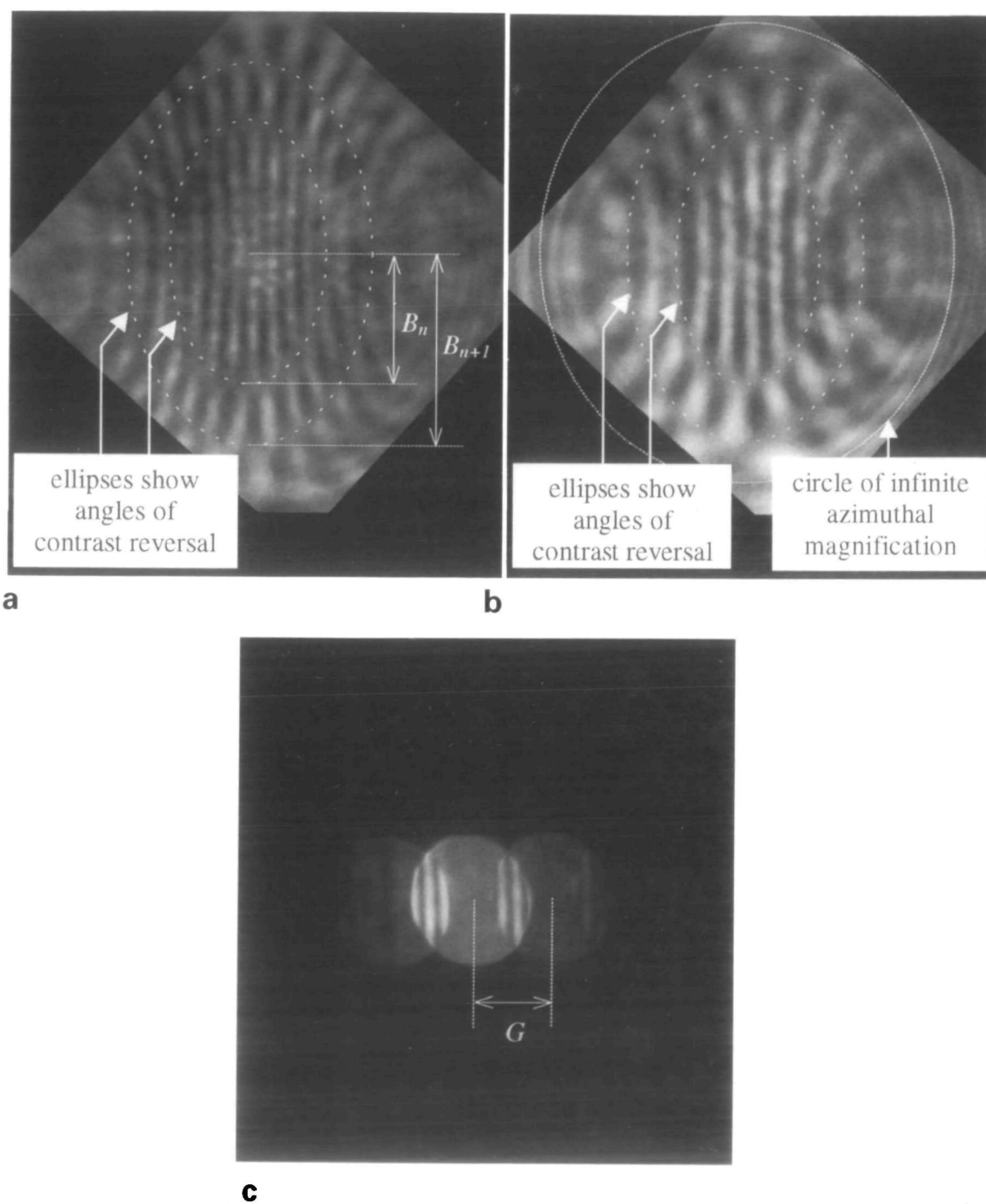


**Fig. 10** (a) Ronchigram of asbestos fibers, formed with a stationary probe at under-focus. The {021} lattice fringes are visible (4.5 Å spacing) and the angles at which their contrast inverts are marked by ellipses. The lengths of the major axes,  $B_n$  and  $B_{n+1}$  are used to evaluate the objective lens spherical aberration coefficient. (b) Ronchigram of asbestos fibers closer to Gaussian focus. The {021} fringes have a larger period than in (a); angles of contrast reversal are indicated with ellipses. At the edge of the figure, the circle of infinite azimuthal magnification is visible (marked with a circle). This feature shows that the Ronchigram is slightly under-focused. (c) Coherent CBED pattern of asbestos {021}, acquired with a small STEM objective aperture and with the same camera length as the Ronchigrams. The spacing,  $G$ , was used to calibrate the angular range of (a) and (b).

environmental conditions and using the same electron-optical settings. Assuming the  $C_S = 0.5$  mm instrument is operated in favourable conditions, and that the STEM lens aberration is not, for some reason, greater than that of the demonstration microscope, the imaging resolution will be as good or superior.

Conventionally, objective lens  $C_S$  is measured by analysing the power spectra of bright-field images, using a specimen such as amorphous Ge. The maxima and minima positions in their characteristic ring patterns (when the image is slightly out of focus) can be used to evaluate the aberration coefficient. In principle, this method can be

used in STEM, since bright-field images are easily acquired with an axial detector. Wong *et al.* have performed this process on a dedicated STEM [39]. However, use of the power spectrum becomes problematic when the spherical aberration coefficient is low ( $\approx 0.5$  mm). The poor counting statistics in STEM bright-field images, due to the level of probe brightness and the low collection angles required, mean that the value cannot be found without a very large percentage error. For this reason, the JEM-2010F STEM  $C_s$  was measured using Ronchigrams as outlined by Lin and Cowley [40].

Ronchigrams are formed with a stationary probe, incident on a thin crystal [41]. The convergence angle is very large (often no STEM objective aperture is used at all) and sets of fringes are visible in the Fraunhofer diffraction plane with distortions characteristic of the specimen periodicity, the lens aberrations and the focus setting. Ronchigrams are extreme examples of coherent CBED patterns.

Figure 10 shows two Ronchigrams where the probe is under-focused with respect to an asbestos fiber. A slow scan CCD camera, attached to a GIF imaging filter, was used for acquisition. Setting the microscope projector lens systems for a very short camera length allowed the ronchigram to be recorded to high enough angles. The observed fringes are due to a  $4.5 \text{ \AA}$  periodicity in the fiber. At certain angles, within the Ronchigram, the bright fringes are seen to suddenly change to dark and *vice versa*. The locus of points where this change occurs forms an ellipse, the major axis of which is  $3^{1/2}$  times the length of the minor axis. If, as in Figure 10, the probe is sufficiently under-focused, a number of ellipses are visible and the fringes continue to be distorted, out to the angle of the Ronchigram circle of infinite magnification [41] (the loci are marked in the figure). Going out in angle, along the ellipses' major axis, the central fringe switches between bright and dark as it traverses each elliptical locus. Lin and Cowley have derived the relationship between consecutive ellipse major axis lengths and the spherical aberration constant of the probe-forming lens:

$$C_s = \frac{(Gd^2)^2}{(B_{n+1}^2 - B_n^2)\lambda^3}, \quad (3)$$

where  $B_n$  is half the major axis of the  $n^{\text{th}}$  ellipse, measured in pixels;  $\lambda$  is the electron wavelength;  $d$  is the crystal lattice spacing; and  $G$  is the spacing of diffraction spots, given by lattice planes of period,  $d$ , in pixels (see Fig. 10c); [40].

From Figs 10a and 10c,  $G = 83$  pixels and  $B_{n+1}^2 - B_n^2 = 3.3 \times 10^4$  square pixels. This gives a value for  $C_s$  of  $0.54$  mm. An error limit of  $\pm 0.1$  mm was estimated. Such a value for the spherical aberration in STEM is, within error, the same as the nominally quoted value. The 'ultra-high resolution' lens must be operating symmetrically at the excitation used for Z-contrast STEM.

## Conclusions

There is a growing body of evidence to suggest that the STEM technique of Z-contrast imaging, in combination with EELS spectrum acquisition, is extremely useful in the characterization of a range of features in crystalline materials right down to the atomic level. This is important since it is the atomic structure at defects and interfaces which is crucial to the understanding of many materials problems. It has been shown that the 200 kV FEGTEM is capable of resolving sub-2 Å spacings in a variety of materials in Z-contrast mode. This is in spite of the use of a Schottky emission source and of the objective lens pre-field to form a probe. A test of the microscope's probe-forming coherence envelope, using a CBED technique, indicates that frequencies corresponding to a specimen spacing of  $1.6 \text{ \AA}$  are passed to the image. In one case, this resolution was just observed in a Z-contrast image of the hexagonal GaN <0001> structure. The spherical aberration coefficient of an ultra-high resolution pole-piece was measured to be just over  $0.5$  mm in STEM operation. Agreement between this value and that quoted by the manufacturer for CTEM indicates the near symmetrical nature of this pole-piece. It is therefore anticipated that the STEM performance of the JEOL JEM-2010F has a limit superior to that established in these preliminary tests, in the demonstration environment. Further development of the microscope's STEM capability, and the ability to operate in a variety of CTEM modes are likely to mean that this instrument will become increasingly useful in atomic resolution analysis of materials.

## Acknowledgements

The authors are grateful for the assistance of JEOL Ltd. and their patience during our use of their demonstration instrument. Image processing software was made available by J. M. Rodenburg at the University of Cambridge, UK, and the strontium titanate specimen was provided by G. Duscher of the Max Planck Institut für Metallforschung in Stuttgart, Germany. This research is funded by the NSF (grant number DMR-9601792) and by the DOE (grant number DE-FG02-96ER45610).

## References

- 1 Reimer L (1997) *Transmission Electron Microscopy* (Springer Verlag, Berlin).
- 2 Hawkes P W and Kasper E (1994) *Electron Optics Vol. 3* (Academic Press, New York).
- 3 Spence J C H (1988) *Experimental High Resolution Electron Microscopy*, 2nd Edition (OUP, New York).
- 4 Xu P R, Kirkland E J, Silcox J, and Keyse R (1990) High-resolution imaging of silicon (111) using a 100 keV STEM. *Ultramicroscopy* **32**: 93–102.
- 5 Pennycook S J, Jesson D E, McGibbon A J, and Nellist P D (1997) High angle dark field STEM for advanced materials. *J. Electron Microsc.* **45**: 36–43.
- 6 Jesson D E and Pennycook S J (1993) Incoherent imaging of thin specimens using coherently scattered electrons. *Proc. R. Soc. (London)* **A 441**: 261–281.

- 7 Jesson D E and Pennycook S J (1995) Incoherent imaging of crystals using thermally scattered electrons. *Proc. R. Soc. (London) A* **449**: 273-293.
- 8 Hartel P, Rose H, and Dingel C (1996) Conditions and reasons for incoherent imaging in STEM. *Ultramicroscopy* **63**: 93-114.
- 9 Nellist P D, Xin Y, and Pennycook S J (1997) Direct structure determination by atomic resolution incoherent STEM imaging. *Inst Phys. Conf. Ser.* **153**: 109-112.
- 10 Egerton R F (1996) *Electron energy-loss spectroscopy in the electron microscope* (Plenum, New York).
- 11 Brown L M (1981) Scanning transmission electron microscopy: microanalysis for the microelectronic age. *J. Phys. F* **11**: 1-26.
- 12 Williams D B and Carter C B (1996) *Transmission Electron Microscopy IV: Spectroscopy* (Plenum, New York).
- 13 Browning N D, Chisholm M F, and Pennycook S J (1993) Atomic resolution chemical analysis using a scanning transmission electron microscope. *Nature (London)* **366**: 143-146.
- 14 Browning N D and Pennycook S J (1996) Direct experimental determination of the atomic structure at internal interfaces. *J. Phys. D Appl. Phys.* **29**: 1779-1798.
- 15 Lakner H, Bollig B, Ungerechts S, and Kubalek E (1996) Characterisation of III-V semiconductor interfaces by Z-contrast imaging, EELS and CBED. *J. Phys. D Appl. Phys.* **29**: 1767-1778.
- 16 Wallis D J, Browning N D, Nellist P D, Pennycook S J, Majid I, Liu Y, and Vander Sande J B (1997) Atomic structure of a  $36.8^\circ$  (210) tilt grain boundary in  $\text{TiO}_2$ . *J. Am. Ceram. Soc.* **80**: 499-502.
- 17 McGibbon M M, Browning N D, Chisholm M F, McGibbon A J, Pennycook S J, Ravikumar V, and Dravid V P (1994) Direct determination of grain boundary atomic structure in  $\text{SrTiO}_3$ . *Science* **266**: 102-104.
- 18 Spence J C H and Cowley J M (1978) Lattice imaging in STEM. *Optik* **50**: 129-142.
- 19 Spence J C H and Zuo J (1992) *Electron Microdiffraction* (Plenum, New York).
- 20 Cowley J M and Moodie A F (1957) The scattering of electrons by atoms and crystals I. A new theoretical approach. *Acta Cryst.* **10**: 609-619.
- 21 Loane R F, Kirkland E J, and Silcox J (1988) Visibility of single heavy atoms on thin crystalline silicon in simulated annular dark-field images. *Acta Cryst. A* **44**: 912-927.
- 22 Hillyard S, Loane R F, and Silcox J (1993) Annular dark-field imaging: resolution and thickness effects. *Ultramicroscopy* **49**: 14-25.
- 23 Hillyard S and Silcox J (1995) Detector geometry, thermal diffuse scattering and strain effects in ADF STEM imaging. *Ultramicroscopy* **58**: 6-17.
- 24 Bollig B, Fischer H G, and Kubalek E (1996) Multislice simulation of high-resolution scanning-transmission electron-microscopy Z-contrast images of semiconductor heterostructures. *Scanning* **18**: 291-300.
- 25 Nakamura K, Kakibayashi H, Kanehori K, and Tanaka N (1997) Position dependence of the visibility of a single gold atom in silicon crystals in HAADF-STEM image simulation. *J. Electron Microsc.* **1**: 33-43.
- 26 Fertig J and Rose H (1981) Resolution and contrast of crystalline objects in high-resolution scanning transmission electron microscopy. *Optik* **5**: 407-429.
- 27 Cowley J M (1969) Image contrast in transmission scanning electron microscopy. *Appl. Phys. Lett.* **15**: 58-60.
- 28 Hawkes P W and Kasper E (1989) *Electron Optics Vol. 2* (Academic Press, New York).
- 29 Fransen M J, Damen E P N, Schiller C, van Rooy T L, Groen H B, and Kruit P (1995) Characterisation of ultrasharp field emitters by projection microscopy. *Appl. Sur. Sci.* **94/95**: 107-112.
- 30 Kruit P (1997) Auger electron spectroscopy in the STEM. *EMAG 97 (Cambridge) Advanced School Proceedings*.
- 31 Xu P (1991) Scanning transmission electron microscopy studies of silicon and epitaxial growth of gold and silver on H-terminated silicon. PhD thesis Cornell University.
- 32 Kawasaki M (1997) Private communication.
- 33 Pennycook S J, Jesson D E, and Browning N D (1995) Atomic resolution electron energy loss spectroscopy in crystalline solids. *Nucl. Instrum. Meth. Phys. Res. B* **96**: 575-582.
- 34 Xin Y, Pennycook S J, Browning N D, Nellist P D, Sivananthan S, Faurie J-P, and Gibart P (1997) Direct observations of atomic structures of defects in GaN by high resolution Z-contrast imaging using STEM. Submitted to MRS, Boston.
- 35 James E M and Rodenburg J M (1997) A method for measuring the effective source coherence in a field emission transmission electron microscope. *Appl. Sur. Sci.* **111**: 174-179.
- 36 Nellist P D and Rodenburg J M (1994) Beyond the conventional information limit: the relevant coherence function. *Ultramicroscopy* **54**: 61-74.
- 37 Midgley P A, Saunders M, and Vincent R (1995) Fourier reconstruction from coherent convergent-beam electron-diffraction patterns. *Inst Phys. Conf. Ser.* **147**: 145-148.
- 38 Zuo J M and Spence J C H (1993) Coherent electron nanodiffraction from perfect and imperfect crystals. *Phil. Mag. A* **68**: 1055-1078.
- 39 Wong K, Kirkland E, Xu P, Loane R, and Silcox J (1992) Measurement of spherical aberration in STEM. *Ultramicroscopy* **40**: 139-150.
- 40 Lin J A and Cowley J M (1986) Calibration of the operating parameters for an HB5 STEM instrument. *Ultramicroscopy* **19**: 31-42.
- 41 Cowley J M (1986) Electron diffraction phenomena observed with a high resolution STEM instrument. *J. Elect. Microsc. Technique* **3**: 25-44.